Near-infrared Real-Time Trace NH_3 Sensor Based on WM-OA-ICOS and EEMD Assisted Optical Denoising

GUOLIN LI,[1,*] YINGJIE ZHAO,[1] YAJING LIU,[1] LONGJU LI,[1] SIYU ZHANG,[1] ENTING DONG,[1] FULI ZHAO,[1] LUPENG JIA,[1] RUIXIANG SUN,[1] HAORAN YUAN,[1] AND GUANGZHAO CUI,[1] CHUANTAO ZHENG[2]

[1]College of Control Science & Engineering, China University of Petroleum (East China), Qingdao 266580, China
[2] State Key Laboratory of Integrated Optoelectronics, College of Electronic Science and Engineering, Jilin University, 2699 Qianjin Street, Changchun, 130012, PR China
**liguolin@upc.edu.cn*

Abstract: In this paper, a near-infrared NH_3 sensor is developed using Wave-length Modulated Off-Axis Integrated Cavity Output Spectroscopy (WM-OA-ICOS) technology. Design a cavity with a length of 15 cm and an effective absorption diameter of 330.5 m. The Ensemble Empirical Mode Decomposition (EEMD) algorithm is adopted as the spectra preprocessing method to reduce the noise, and Allan deviation analysis is conducted by comparing the original signal. It is found that the limit of detection (LoD) of the sensor could reach ~1.54 ppb with an integration time of 43 s. The concentration calibration experiment shows that the sensor can achieve double range. To enhance accuracy and sensitivity in NH_3 concentration inversion, the Cuckoo Search algorithm with the Elman neural network (CS-Elman) was designed. Through experimental validation, the sensor achieves rapid detection of trace NH_3. The outstanding performance of the NH_3 detection device in monitoring trace gases has been demonstrated by field deployment trials.

1. Introduction

Ammonia(NH_3) is an inorganic compound, a colorless gas with a strong irritating odor. Agricultural emissions represent one of the primary sources of NH_3 in the atmosphere [1-3]. Since the 1980s and 1990s, three catalysts have been added to gasoline, increasing NH_3 emissions in urban environments. The United States Department of Labor Occupational Safety and Health Administration (OSHA) regulations of indoor NH_3 allowable concentration of 50 ppm. The Indoor Air Quality Standard stipulates that the maximum allowable concentration of NH_3 in indoor air is 0.2 mg/m^3 (0.2635ppm); The maximum allowable concentration of harmful substances in the air of the workshop in the Health Standard for Industrial Enterprise Design is 30 mg/m^3 (39.53ppm) of NH_3. As can be seen from the above emission standard requirements, the NH_3 concentration range detected in the indoor air should be 0~10 ppm, and the NH_3 concentration range detected in the workshop air should be 0~100 ppm. Therefore, the development of an efficient, real-time, and high-precision NH_3 detection sensor is essential to ensure public health [4]. However, the concentration of NH_3 gas in the air is extremely low, so it is necessary to develop an efficient, real-time, and high-precision NH_3 sensor for atmospheric detection.

With the rapid development of laser spectroscopy, many techniques are widely used for trace gas detection, such as: Tunable Diode Laser Absorption Spectroscopy, Cavity Ring-down Spectroscopy, and Cavity-enhanced Absorption Spectroscopy (CEAS). Among them, CEAS technology has received widespread attention for its robustness, high detection accuracy and fast analysis speeds. OA-ICOS technology originated from CEAS technology [5]. It effectively reduces the interference and fluctuations caused by multiple reflections of light in the cavity [6-9], and the cavity mode noise is effectively suppressed. Moreover in the case of off-axis incidence, the energy of the original single fundamental mode is distributed among many higher-order transverse modes, which results in very weak output power detected by the detector Improving the device's signal-to-noise ratio (SNR) is challenging due to limitations in laser power and detector sensitivity. Therefore, introducing wavelength modulation spectroscopy [10-11] can effectively suppress low-frequency noise and further improve the SNR of the sensor.

In 2002, an OA-ICOS instrument based on a DFB diode laser was reported for sensitive CO measurement. In the integration time of 50 seconds, the minimum detectable absorptivity when the effective optical path is 4.2 km is 3.1×10^{-11} cm^{-1} $Hz^{-1/2}$ [12]. In 2004, Bakhirkin et al. used Wave-length modulated off-axis integrating cavity output spectroscopy (WMS-OA-ICOS) and OA-ICOS techniques respectively to detect the concentration of NO in respiratory gas, and the experiment found that the sensitivity of the former was 5 times that of the latter l971 [13]. In 2012, Malara et al. used OA-ICOS and WMS-OA-ICOS to measure the concentration of CH_4 in the atmosphere, and found that WMS-OA-ICOS was mainly affected by the laser scanning frequency, and the enhancement multiple was related to the reflectivity of the cavity mirror used [14]. An increased absorption path is achieved by most reported OA-ICOS systems by using a longer cavity length (> 30 cm). However, the increased cavity length, while facilitating longer absorption paths, also poses challenges for system integration and beam coupling within the cavity. At the same time, they did not discuss the inversion of weak signal concentration.

In this paper, a small 15 cm detachable cavity is designed. A DFB laser with an emission wavelength of 1531.7nm was selected, specifically targeting the NH_3 absorption line located at 6528.27cm^{-1}. Simultaneously, in order to effectively suppress low-frequency noise, combining WMS and OA-ICOS techniques. The data processing system is based on the LabVIEW platform. It is composed of orthogonal phase-locked amplifier module, signal acquisition module, and scanning modulation signal generation module. This enables the sensor to perform routine operations including DFB laser actuation and also to acquire NH_3 harmonic signals from absorption spectra using a laptop and data acquisition card (DAQ). Using EEMD technique to pre-process the raw signals of ammonia spectra. In order to improve the sensitivity and accuracy of NH_3 concentration inversion, a method combining the Cuckoo search algorithm (CS) and Elman neural network is designed. It has higher test accuracy and anti-interference compared with other detection sensors. The sensor can be used for atmospheric environment measurement, which has important application value for the detection of NH_3 in atmospheric environment.

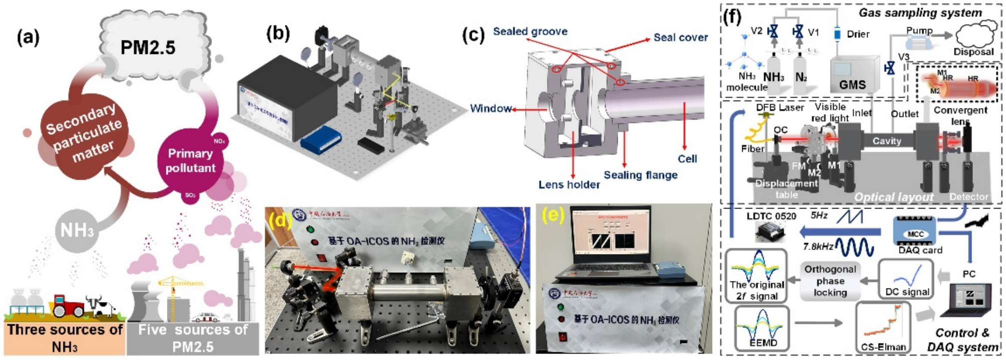

Fig. 1. (a) Sources of NH_3; (b) Sensor side view; (c) The main structure of the cavity; (d) Optical path structure of NH_3 detection sensor based on OA-ICOS; (e) Photograph of the NH_3 sensor; (f) Diagram depicting the NH_3 detection sensor utilizing a virtual instrument platform.

Sensor Configuration

The main sources of NH_3 in the atmosphere and the main components of haze are shown in Fig. 1(a). In order to measure the content of ammonia in the atmosphere, an ammonia detection sensor is built. Fig. 1(b) are structural diagrams of the detection device. Fig. 1(d) shows the optical part. The sensor diagram is shown in Fig. 1(e). As shown in Fig. 1(f), the gas processing part, the optical part, and the electrical part are included in the experimental setup.

In the optical part, use Solidworks to design the removable cavity, through the sealing flange for sealing and fixing the cavity and the main frame, to avoid the error caused by the displacement of the cavity in the welding process, the total length of the cavity is 150 mm, the overall structure is shown in Fig. 1(c). After testing, the cavity sealing and stability is better.

The absorption spectrum of NH_3 gas in the range of 5882.35~6666.67cm^{-1} is shown in Fig. 2(a). In order to eliminate interference from H_2O and CO_2, the NH_3 absorption peak with low interference at a center wavelength of 6528.27cm^{-1} was selected as the best target line. Simulation of the absorption spectra of 1 ppm NH_3 and ambient concentrations of H_2O and CO_2, as depicted in Fig. 2(b). Among them, the low interference NH_3 absorption peak centered at 6528.27 cm^{-1} was identified as the optimal absorption line. Therefore, using a 1531.7 nm DFB laser to detect NH_3, lock the NH_3 absorption line at 6528.27cm^{-1}. The relationship between optical power and wavelength under different driving currents is measured. The measured W-I (wavelength-current) and P-I (power-current) curves are shown in Fig. 2(c).

In the electrical part, it mainly consists of three electronic components: a laptop computer (LENOVO, YOGA710), a DAQ card (Measurement Computing, USB-1808X), and a constant current source module (Wavelength Electronics, LDTC0520). The analog output module of the data acquisition card controlled by LabVIEW generates a combined waveform of a high frequency sine wave (7.8 kHz) and a low frequency sawtooth wave (5 Hz), which provides a current source to make the DFB laser emit light. The Quadrature lock-in amplifier and memory module developed on the LabVIEW platform reduce noise by processing 10 times the average. In the sensor, EEMD and CS-Elman algorithms are integrated respectively for spectrum preprocessing and concentration inversion.

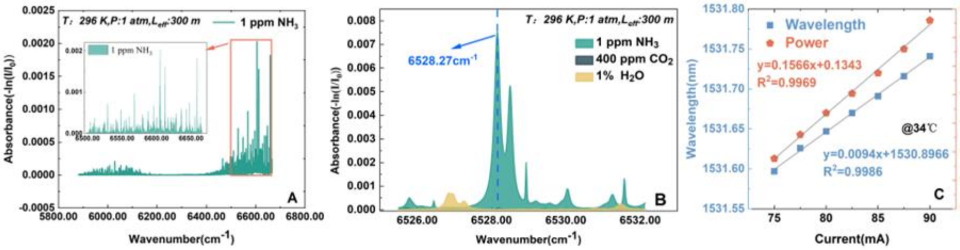

Fig. 2. (a) Absorption bands of 1 ppm NH_3 in the range of 6500cm^{-1} to 6666cm^{-1} at 1 atm, 296K, and 300 m optical paths; (b) Absorption lines of 1 ppmNH_3, 1% H_2O, 400 ppm CO_2 at 6528.27 cm^{-1} at 1 atm, 296K and 300 m optical path; (c) Graph of response of current to wavelength and optical power.

Optical and 1/f noise processing

3.1 Cavity mode noise processing

A key challenge in the output absorption spectroscopy of off-axis integrating cavities lies in the signal interference caused by light intensity fluctuations due to interference in F-P cavities, a phenomenon commonly referred to as cavity mode noise, which significantly limits the high sensitivity performance of the system [15]. Assuming that N is the number of lasers coupled into the cavity per second at an integration time T, the signal collected by the detector contains TN transmission peaks; when the frequency of the scanning signal is f and the number of couplings into the cavity is n, the number of laser couplings into the cavity per second is N=2fn. The relative dispersion ξ of a single transmission peak is related to the laser modulation frequency, which takes values between 0.15 and 0.5 for the noise magnitude [16]:

$$\delta = \frac{\Delta I}{I} = \xi\sqrt{\frac{1}{NT}} = \xi\sqrt{\frac{1}{2fnt}}, \tag{1}$$

Then increasing the mode of the laser in the optical resonant cavity reduces the cavity film noise, which can be achieved by using off-axis incidence. In order to ensure that the beam can be reflected repeatedly in the cavity when using off-axis incidence, the re-entrant condition must be met, when the number of cavity moulds is enough, the result of integrating the cavities can be analogous to a Herriott or White pool,an ellipse-like pattern is formed on the lens. In the case of satisfying the resonant cavity stability condition, the re-entrant condition is expressed as:

$$\begin{cases} 2m\theta = 2n\pi \\ \cos(2\theta) = 1 - \dfrac{L}{r} \end{cases}, \tag{2}$$

When n is set to an integer, the FSR is 1/m times the original, and the value of m is affected by both spot size and lens size. In the case of off-axis incidence, when the FSR is close to zero, the mode density inside the cavity rises sharply, making the light propagation nearly continuous, and the original cavity mode structure is almost difficult to be recognised. Under this situation, the cavity mode noise is effectively suppressed.

After off-axis processing, the system will still have some residual cavity mode noise and because the output signal from the off-axis integrating cavity is weak, the absorption spectrum detected by the detector is weak and often accompanied by random noise, which distorts the ammonia spectrum and affects the detection limit of the sensor. In order to enhance the robustness of the sensor, pre-processing of the raw signals obtained from the ammonia spectra is essential, and this process can be implemented by relying on techniques and algorithms of digital signal processing。In this paper applying the EEMD (Ensemble Empirical Mode Decomposition) technique [17-18].

The EEMD [19-23] decomposition steps are as follows:

(1) The overall average number M is defined.

(2) To generate a new signal, a standard plus distribution of white noise is added to the original signal.

$$x_i(t) = x(t) + n_i(t), i = 1, 2, ...M, \tag{3}$$

In the equation, $n_i(t)$ is the original signal. is representative of the i-th addition of white noise sequence, while $x_i(t)$ denotes the i-th experimental attachment of noise signal

(3) The resulting noise signals are decomposed separately by EMD, and the forms of their respective IMF sums are obtained:

$$x_i(t) = \sum\nolimits_{j=1}^{J} g_{i,j}(t) + r_{i,j}(t), \tag{4}$$

In the equation, $g_{i,j}(t)$ is the j- th IMF, $g_{i,j}(t)$ decomposed after adding white noise for the i-th time. It represents the residual function, which is the average trend of the signal. J is the number of IMFs.

(4) Iteratively perform steps (2) and (3) M times, incorporating varying amplitudes of white noise into each decomposition to derive the set of IMF:

$$\begin{aligned} &g_{1,j}(t), g_{2,j}(t), g_{3,j}(t)...g_{M,j}(t), \\ &j = 1, 2, ...J \end{aligned} \tag{5}$$

(5) The above corresponding IMF sets are averaged, and by adopting the principle that the average value of uncorrelated sequences is zero, the IMF decomposed by EEMD is finally obtained, that is:

$$g_j(t)=\frac{1}{M}\sum\nolimits_{i=1}^{M}g_{i,j}(t), i=1,2,...M, j=1,2,...J, \tag{6}$$

In the formula, $g_j(t)$ is the jth IMF decomposed by EEMD.

3.2 1/f noise processing

In the case of off-axis incidence, the energy of the original single fundamental mode is distributed into many higher-order transverse modes,lead to the output power detected by the detector is very weak, and the signal-to-noise ratio of the device is difficult to improve due to the limitation of the laser power and the sensitivity of the detector. Lasers and detectors will introduce 1/f noise into the measurement results, and the characteristics of this noise is that the lower the frequency, the higher the noise, so the introduction of wavelength modulation spectroscopy (WMS) to effectively suppress the low-frequency noise, and further improve the sensor signal-to-noise ratio.

When the laser is injected with a sinusoidal modulated current of frequency f, the laser's emitted light intensity and wave number change at the same time, and the light intensity $I_0\left(t\right)$ and wave number $v\left(t\right)$ can be expressed as follows:

$$\begin{aligned} I_0\left(t\right)&=G\overline{I_0}\left[1+\sum_{k=1}^{\infty}i_k\cos\left(k\cdot 2\pi ft+\psi_k\right)\right], \\ v\left(t\right)&=v_1+\sum_{n=1}^{\infty}a_n\cos\left(2\pi ft+\varphi_n\right) \end{aligned} \tag{7}$$

G denotes the amplification factor of the detector; I_0 represents the intensity of the laser light when unmodulated; i_k is the Fourier coefficient for k modulations of the laser intensity; ψ_k represents the phase change of the modulated light intensity of the kth order; v_1 represents the centre wavelength of the laser emission; a_n represents the depth of the nth modulation; φ_n represents the phase corresponding to the nth modulation.

The spectral absorptivity $\alpha\left(t\right)$, can be expanded according to the Beer-Lambert law into a Fourier series with frequency f as the fundamental frequency:

$$\alpha\left(t\right)=\sum_{k=0}^{\infty}\left[M_k\cos\left(k\cdot 2\pi ft\right)+N_k\sin\left(k\cdot 2\pi ft\right)\right], \tag{8}$$

M_k and N_k are the kth Fourier coefficients, denoted as

$$\begin{aligned} M_k&=\frac{1}{\left(1+\delta_0\right)\pi}\int_{-\pi}^{\pi}\tau\left[v_1+\sum_{n=0}^{\infty}a_n\cos\left(n\cdot 2\pi ft+\varphi_n\right)\right]\cos k\theta d\theta, \\ N_k&=\frac{1}{\left(1+\delta_0\right)\pi}\int_{-\pi}^{\pi}\tau\left[v_1+\sum_{n=0}^{\infty}a_n\cos\left(n\cdot 2\pi ft+\varphi_n\right)\right]\sin k\theta d\theta \end{aligned} \tag{9}$$

Using digital phase-locking technology to obtain the harmonic signals of light intensity at a specific modulation frequency, separate the light intensity signals and demodulate them by multiplying by cos(n) and sin(n), using a low-pass filter to filter out high-frequency noise to obtain the X and Y components of the nth harmonic signal, to provide a reliable basis for subsequent data analysis and processing.

$$\begin{aligned} X_{nf}&=\frac{G\overline{I_0}}{2}\left\{M_n+\frac{1}{2}\sum_{k=1}^{\infty}\left[M_{n+k}+\left(1+\delta_{nk}\right)M_{|n-k|}\right]i_k\cos\left(\varphi_k\right)-\frac{1}{2}\sum_{k=1}^{\infty}\left[N_{n+k}-\operatorname{sgn}\left(n-k\right)N_{|n-k|}\right]i_k\sin\left(\varphi_k\right)\right\}, \\ Y_{nf}&=\frac{G\overline{I_0}}{2}\left\{\frac{1}{2}\sum_{k=1}^{\infty}\left[M_{n+k}-\left(1+\delta_{nk}\right)M_{|n-k|}\right]i_k\sin\left(\varphi_k\right)+\frac{1}{2}\sum_{k=1}^{\infty}\left[N_{n+k}+\operatorname{sgn}\left(n-k\right)N_{|n-k|}\right]i_k\cos\left(\varphi_k\right)\right\} \end{aligned} \tag{10}$$

When there is no absorption that means m=n and n=0, we substitute to get:

$$X_{nf}^{0} = \frac{G\overline{I_0}}{2} i_n \cos(\varphi_n),$$
$$Y_{nf}^{0} = -\frac{G\overline{I_0}}{2} i_n \sin(\varphi_n) \tag{11}$$

Compare and represent the raw harmonic amplitude with the harmonic amplitude after subtracting the background:

$$R_{nf} = \sqrt{X_{nf}^2 + Y_{nf}^2},$$
$$S_{nf} = \sqrt{\left(X_{nf} - X_{nf}^0\right)^2 + \left(Y_{nf} - Y_{nf}^0\right)^2} \tag{12}$$

Perform a normalisation operation to deduct the harmonic amplitudes in the background signal:

$$S_{nf/1f} = \sqrt{\left(\frac{X_{nf}}{R_{1f}} - \frac{X_{nf}^0}{R_{1f}^0}\right)^2 + \left(\frac{Y_{nf}}{R_{1f}} - \frac{Y_{nf}^0}{R_{1f}^0}\right)^2}, \tag{13}$$

From the above equation, the harmonic amplitude obtained is mainly related to the absorption, which effectively improves the sensor signal-to-noise ratio, and the subsequent use of phase-locked amplifiers for harmonic signal extraction.

2. Performance verification

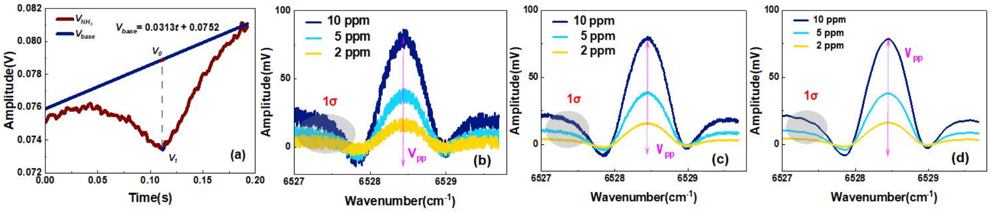

Fig. 3. (a) Absorption spectra of NH_3 near 6528.27cm^{-1} and fitting baseline; (b) Sensor-recorded raw 2f signals; (c) Signals recorded and filtered using EMD; (d) Signals recorded and filtered using EEMD.

TABLE 1. SNR Comparison

Algorithms	SNR		
	10 ppm	5 ppm	2 ppm
Raw 2f signal	16.49	14.57	12.05
EMD	35.27	30.05	24.27
EEMD	53.57	51.49	50.26

4.1 Calibration of effective optical path length and cavity mirror reflectivity

To determine the effective optical path length and calibrate the mirror reflectivity of the cavity, a 5hz sawtooth signal is used for scanning. A 1531.7 nm DFB was used to lock the NH_3 absorption line at 6528.27 cm^{-1}, with a NH_3 sample concentration level of 10 ppmv introduced into the off-axis integrated cavity. As shown in Fig. 3(a), the differential signal can be obtained by subtracting the background-fitted signal from the absorption signal. The maximum absorption occurs at t=0.11 s, with an absorption signal corresponding to a voltage of 0.073 V, and a voltage of 0.079 V at non-absorption regions. The output voltage, input current, and output optical power all exhibit linear response with acquisition time, so absorbance (A) can be calculated using equation 14.

$$A = -\ln\left(\frac{V_1}{V_0}\right), \tag{14}$$

The absorbance was determined to be 0.0789 by calculation. According to the HITRAN molecular absorption database, the actual total optical path length is determined to be 330.5 m. Using the actual optical path length, the effective reflectivity of the high-reflectance mirror can be reverse-engineered. Through computation, the calibrated reflectivity of the cavity mirror is found to be 99.95%.

4.2 Filtering performances using EEMD signal-processing

In order to test the practical denoising effect of the EEMD algorithm, partial gas experiments were first conducted, and the original 2f signals were collected and compared with the filtered signals to evaluate their SNR. N_2 gas with NH_3 concentrations of 10, 5, and 2 ppmv was detected using an automated gas distribution system. The collected original signals, EMD-filtered signals, and EEMD-filtered signals are shown in Fig. 3.(b) (c) and (d). The original signal contains obvious noise as can be seen from Figure 8. The SNR of the original 2f signals and the denoised 2f signals after EEMD filtering are calculated according to the formula and presented in Table I. Compared to the original signals, the SNR of the signals after EEMD filtering is significantly improved to varying degrees, indicating the effectiveness and superiority of this filtering algorithm in noise reduction.

4.3 Concentration inversion calibration and data fitting

The concentration calibration experiment utilized an automated gas distribution station with N_2 as carrier gas and dynamic mixing of NH_3 in the concentration range of 10~100 ppm and 0.4~10 ppm. During the calibration process, the gas progresses from lower experimental concentrations, with gradients and spectra processed by algorithms as shown in Fig. 4(a) and (b) respectively, while the relationship between average voltage and gas concentration is depicted in Fig. 4(c) and (d).

Fig. 4(c) shows the sensor's exceptional linearity concerning NH_3 within the concentration range of 0.4 ~ 10 ppm, yielding a robust linear relationship between NH_3 concentration and the 2f peak value. The combined linear coefficient R^2 achieves a remarkable value of 0.9993, which is expressed as follows:

$$y = 7.6769 \times Max\left(2f\right) + 1.1606, \tag{15}$$

Furthermore, the linear relationship for the concentrations ranging of 10 ~ 100 ppm is illustrated by Fig. 4(d), with the linear coefficient R^2 reaching 0.9981. Through curve fitting, the relationship between concentration and 2f peak can be expressed as follows:

$$y = 10.142 \times Max\left(2f\right) + 0.3802, \tag{16}$$

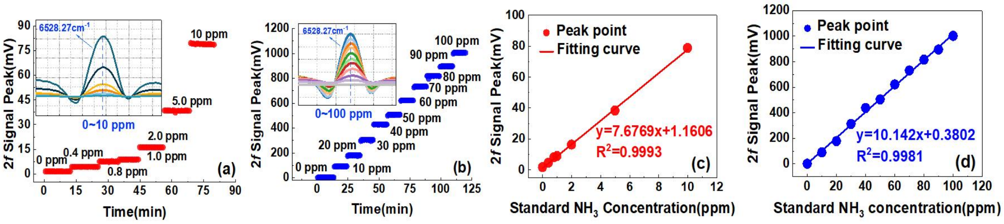

Fig. 4. (a) 0.4~10 ppm NH_3 concentration gradient and measured spectra; (b) 10~100 ppm NH_3 concentration gradient and measured spectra; (c) 0.4~10 ppm 2f amplitude and concentration linear fitting curve; (d) 10~100 ppm 2f amplitude and concentration linear fitting curve.

4.4 Comparison of concentration inversion algorithm results

In this paper, the inversion model is provided by the Elman neural network [24-27]. To solve the slow training and potential local minimum trap while improving the generalization performance, the initial weights and thresholds of the network are optimized by the Cuckoo Search (CS) algorithm [28]. Finally, the concentration inversion prediction model of CS-Elman neural network (CS-Elman) is established.

The concentration inversion was performed for the 2f signal of NH_3 in the range of 0 ~ 10 ppm and 0 ~ 100 ppm. The concentration retrieval performance of CS-Elman, BPNN, LSSVM and Elman algorithms is compared. NH_3 gas spectra were modeled using a five-fold cross-validation approach across both concentration ranges. Four folds were dedicated to training, leaving one for validation. The outcomes of this five-fold cross-validation method are demonstrated in Fig. 5(a) and (c), with the prediction results shown in Fig. 5(b) and (d). The predicted concentrations by the CS-Elman algorithm are closest to the true values with the smallest absolute error.

Comparison results of linear correlation coefficient R^2, root mean square error (RMSE), and standard deviation between the predicted and actual concentrations obtained by different algorithms are shown in Table II and III. Error analysis after processing by the CS-Elman algorithm showed an improvement of 2 to 4 times compared to the other three algorithm models.

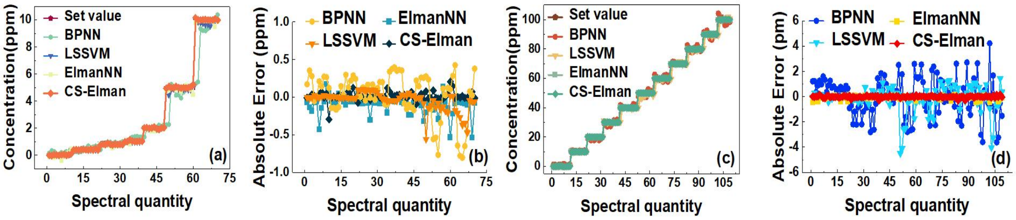

Fig. 5. (a) Comparison chart of predicted values and set values of BPNN, LSSVM, ElmanNN and CS-Elman algorithms are in the range of NH_3 concentration from 0 to 10 ppm; (b) Comparison of error between standard concentration and measured concentration for BPNN, LSSVM, ElmanNN, and CS-Elman algorithms at concentrations of 0~10 pm; (c) Comparison plots of predicted values and set values of BPNN, LSSVM, ElmanNN and CS-Elman algorithms are in the range of NH_3 concentration from 0 to 100 ppm; (d) Comparison of error between standard concentration and measured concentration for BPNN, LSSVM, ElmanNN, and CS-Elman algorithms at concentrations of 0~100 ppm.

TABLE 2. Comparison of Fitting Accuracy of Four Algorithms at 0~10 ppm NH_3 Concentration

Algorithms	Standard deviation(ppm)	RMSE (ppm)	R^2
BPNN	0.268	1.865	0.9982
LSSVM	0.015	0.098	0.9991
ElmanNN	0.025	0.156	0.9997
CS-Elman	0.004	0.061	0.9999

TABLE 3. Comparison of Fitting Accuracy of Four Algorithms at 0~100 ppm NH_3 Concentration

Algorithms	Standard deviation(ppm)	RMSE (ppm)	R^2
BPNN	1.015	2.415	0.9975
LSSVM	0.108	1.096	0.9993
ElmanNN	0.003	0.052	0.9995
CS-Elman	0.001	0.035	0.9998

4.5 Sensor stability

The stability, resolution and limit of detection (LoD) of the sensor are verified by experiments. A standard concentration of 20 ppm NH_3 was provided by an automatic gas distribution station and pumped into the off-axis integration cavity for gas detection. Concentration measurements were then recorded over a 90-minute period. The results are depicted in Fig. 6. The unfiltered NH_3 concentration is shown in Fig. 6(a). The concentration fluctuated between 19.905~20.107 ppm with a standard deviation of 0.0417 ppm. Fig. 6(b) shows that after EEMD filtering, the NH_3 concentration is between 19.951~20.041 ppm, with a maximum fluctuation error of 0.0898 ppm and a standard deviation of 0.0107 ppm. The Allen variance without using the preprocessing algorithm is shown in Fig. 6(c) with an integration time of 49 s and a theoretical

LoD of 5.14 ppb for the sensor. After spectral preprocessing algorithms were applied, it is indicated by Fig. 6(d) that, with an integration time of 1 s, the LoD is measured at 10.35 ppb, and when the integration time is 43 s, the LoD is increased to 1.54 ppb. This shows that the LoD has been significantly improved after EEMD processing, and the sensor has high stability and SNR in long-term operation.

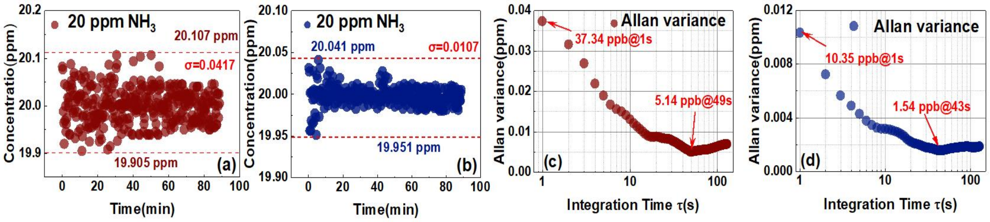

Fig. 6. (a) Long-term stability data of the original signal 2f signal; (b) Long-term stability data after EEMD processing; (c) Allan variance analysis of the original 2f signal; (d) Allan variance analysis after EEMD processing.

4.6 Field Application

The air was continuously measured for 90 min, and the gas concentration detected in real time was shown in Fig. 7. The ammonia concentration fluctuated in the range of 400~800 ppb. In view of the sudden rise in NH_3 concentration, it is speculated that the chemical laboratory on the same floor is carrying out chemical experiments. Field experiment results show that the device has excellent performance in monitoring trace gases.

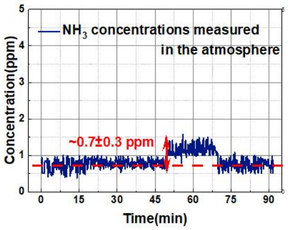

Fig. 7. NH_3 trace detection sensor deployed on site.

3. Conclusion

In this paper, a near-infrared WM-OA-ICOS sensor is demonstrated, suppression of cavity mould noise through the use of off-axis methods and suppressing 1/f noise by introducing WMS, integrates a spectral denoising algorithm and a concentration inversion model to enable continuous real-time detection of NH_3 was developed. Experimentally verified the sensor has a compact structure with an effective absorption length of 330.5 m. The EEMD algorithm is used as a spectral preprocessing method to effectively remove the noise in the 2f signal. In order to improve the accuracy and sensitivity of NH_3 concentration inversion, a method combining the CS algorithm and Elman neural network is designed. After 90 min of long-term stability experiments, the standard concentration of NH_3 is 20 ppm, the concentration value is between 19.951~20.041 ppm. NH_3 concentration analysis is then conducted using the Allan deviation method, revealing the LoD of ~1.54 ppb and an average detection time of 43 s. In addition, the OA-ICOS sensor was tested in an outdoor laboratory and its stability in monitoring atmospheric gases was further confirmed by 1 hour of ambient NH_3 monitoring.

Disclosures. The authors declare no conflicts of interest.

Acknowledgments. This work is supported by the Shandong Province Technology Innovation Guidance Program 2020SDGJZDBZ02, the National Natural Science Foundation of China 62205378, the Beijing Municipal Key Project Outsourcing HX20211125, and the National Key Research and Development Program of China 2020YFB0408402.

References

1. S. H. Chen, M. M. Cheng, Z. Guo, et al., "Enhanced atmospheric ammonia (NH_3) pollution in China from 2008 to 2016: Evidence from a combination of observations and emissions," Environmental Pollution. 263, 114421 (2020).
2. M. Lei, TH Cheng, XY Li, et al., "Atmospheric ammonia point source detection technique at regional scale using high resolution satellite imagery and deep learning," Atmospheric Research. 257, 105587 (2021).
3. Z. R. Lan, W. L. Lin, G. Zhao, "Sources, Variations, and Effects on Air Quality of Atmospheric Ammonia," Current Pollution Reports.10, 40-53 (2024).
4. P. Liu, J. Ding, L. Liu, et al., "Estimation of surface ammonia concentrations and emissions in China from the polar-orbiting Infrared Atmospheric Sounding Interferometer and the FY-4A Geostationary Interferometric Infrared Sounder," Atmospheric Chemistry and Physics. 22, 9099-9110 (2022).
5. R. Centeno, J. Mandon, S. M. Cristescu, et al., "Sensitivity enhancement in off-axis integrated cavity output spectroscopy," Optics Express. 22, 27985-27991 (2014).
6. J. J. Wang, X. Tian, Y. Dong, et al., "Enhancing off-axis integrated cavity output spectroscopy (OA-ICOS) with radio frequency white noise for gas sensing," Optics Express. 27, 30517-30529 (2019).
7. R. Centeno, J. Mandon, S. M. Cristescu, et al., "Three mirror off axis integrated cavity output spectroscopy for the detection of ethylene using a quantum cascade laser," Sensors and Actuators B-Chemical. 203, 311-319, (2014).
8. K. Y. Zheng, C.T. Zheng, H.P. Zhang, et al., "A novel gas sensing scheme using near-infrared multi-input multi-output off-axis integrated cavity output spectroscopy (MIMO-OA-ICOS)," Spectrochimica Acta Part a-Molecular and Biomolecular Spectroscopy. 256, 119745 (2021).
9. G. Y. Guan, A.Q. Liu, X.Y. Wu, et al., "Near-Infrared Off-Axis Cavity-Enhanced Optical Frequency Comb Spectroscopy for CO_2/CO Dual-Gas Detection Assisted by Machine Learning," Acs Sensors. 9, 820-829 (2024).
10. M.-N. Ngo, Tong N.-B, Dorothée Dewaele, et al., "Wavelength modulation enhanced off-axis integrated cavity output spectroscopy for OH radical measurement at 2.8 µm," Sensors and Actuators A: Physical. 362, 114654 (2023).
11. J. J. Wang, X. Tian, Y. Dong, et al., "High-sensitivity off-axis integrated cavity output spectroscopy implementing wavelength modulation and white noise perturbation," Optics Letters. 44, 3298-3301 (2019).
12. D. S. Baer, J. B. Paul, J. B. Gupta, et al., "Sensitive absorption measurements in the near-infrared region using off-axis integrated-cavity-output spectroscopy," Applied Physics B-Lasers and Optics. 75, 261-265 (2002).
13. Y. A. Bakhirkin, A. A. Kosterev, C. Roller, R. F. Curl, et al., "Mid-infrared quantum cascade laser based off-axis integrated cavity output spectroscopy for biogenic nitric oxide detection," Applied Optics. 43, 2257-2266, (2004).
14. P. Malara, M. F. Witinski, F. Capasso, et al., "Sensitivity enhancement of off-axis ICOS using wavelength modulation," Applied Physics B-Lasers and Optics. 108, 353-359 (2012).
15. Morville J, Romanini D, Chenevier M, et al., "Effects of laser phase noise on the injection of a high-finesse cavity," Applied Optics. 41, 6980-6990 (2002).
16. Zybin A, Kuritsyn Y A, Mironenko V R, et al., " Cavity enhanced wavelength modulation spectrometry for application in chemical analysis," Applied Physics. 78, 103-109 (2004).
17. Zhang H, Feng L, Wang J, et al., "Development of technology predicting based on EEMD-GRU: An empirical study of aircraft assembly technology," Expert Systems with Applications. 246, 123208 (2024).
18. Z Dao F, Zeng Y, Qian J, "A novel denoising method of the hydro-turbine runner for fault signal based on WT-EEMD," Measurement. 219, 113306 (2023).
19. H. Y. Zhang, L. J. Feng, J. F. Wang, et al., "Development of technology predicting based on EEMD-GRU: An empirical study of aircraft assembly technology," Expert Systems with Applications. 246, 123208 (2024).
20. F. Dao, Y. Zeng, J. Qian, "A novel denoising method of the hydro-turbine runner for fault signal based on WT-EEMD," Measurement. 219, 113306 (2023).
21. D. Li, M. R. Jiang, M. W. Li, et al., "A floating offshore platform motion forecasting approach based on EEMD hybrid ConvLSTM and chaotic quantum ALO," Applied Soft Computing. 144, 110487 (2023).
22. Y. K. Lu, B. Y. Sheng, G. C. Fu, et al., "Prophet-EEMD-LSTM based method for predicting energy consumption in the paint workshop," Applied Soft Computing. 143, 110447 (2023).
23. H. Su, N. Zhou, Q. S. Wu, et al., "Investigating price fluctuations in copper futures: Based on EEMD and Markov-switching VAR model," Resources Policy. 82, 103518 (2023).
24. Y. Guo, D. F. Yang, Y. Zhang, et al., "Online estimation of SOH for lithium-ion battery based on SSA-Elman neural network," Protection and Control of Modern Power Systems. 7, 40 (2022).
25. Y. Zhang, J. P. Zhao, L. M. Wang, et al., "An improved OIF Elman neural network based on CSO algorithm and its applications," Computer Communications. 171, 148-156 (2021).
26. X. Y. Ma, X. H. Zhang, "A short-term prediction model to forecast power of photovoltaic based on MFA-Elman," Energy Report. 8, 495-507 (2022).
27. M. Zhang, J. X. Yang, R. F. Ma, et al., "RETRACTED: Prediction of small-scale piles by considering lateral deflection based on Elman Neural Network-Improved Arithmetic Optimizer algorithm (Retracted Article)," Isa Transactions. 127, 473-486 (2022).
28. R. Rajabioun, "Cuckoo Optimization Algorithm," Applied Soft Computing. 11, 5508-5518 (2011).